Earth and Planetary Science Letters ••• (••••) •••–•••

Contents lists available at ScienceDirect

Earth and Planetary Science Letters

www.elsevier.com/locate/epsl

A method for mapping crustal deformation and anisotropy with receiver functions and first results from USArray

Vera Schulte-Pelkum [a,b,*], Kevin H. Mahan [b]

[a] Cooperative Institute for Research in Environmental Sciences, 2200 Colorado Ave., University of Colorado Boulder, Boulder, CO 80309-0399, USA
[b] Department of Geological Sciences, University of Colorado Boulder, Boulder, CO 80309-0399, USA

ARTICLE INFO

Article history:
Accepted 30 January 2014
Available online xxxx
Editor: P. Shearer

Keywords:
receiver functions
crustal anisotropy
lithospheric deformation
ductile fabric
foliation strike

ABSTRACT

Lithosphere that has undergone deformation may record this process in the form of fabric such as foliation and lineation from ductile deformation, as well as non-horizontal interfaces between materials with different properties within the crust or at the bottom of the crust (Moho). The receiver function analysis technique isolates teleseismic mode conversions originating at velocity contrasts beneath a seismic station. We show that dipping isotropic contrasts as well as small (<10%) anisotropy generate first-order (i.e. Moho-sized) arrivals in receiver functions. We demonstrate that the azimuthally varying signal can be isolated from radial component receiver functions by subtracting the average (degree 0) over backazimuth. The radial signal matches the tangential component signal with an offset of 90° in backazimuth in the case of isotropic dipping interfaces or plunging axis anisotropy, with both dominated by a degree-1 variation in backazimuth. The positions of the extrema and nodes in both components constrain the strike of the dipping interface, dipping foliation, or plane perpendicular to a fast lineation. For azimuthal anisotropy, the offset between components is 45° and both show a degree-2 azimuthal variation. A distinction between isotropic dipping interfaces and plunging axis anisotropy can be made via the lack of a polarity-reversed azimuthal variation of the direct arrival in the anisotropic case. The described behavior is independent of fast versus slow axis symmetry and absolute velocities and largely independent of strength of anisotropy, exact anisotropic symmetry such as shape factor, and interface or foliation dip. Our method simply consists of subtracting the station average from the radial component receiver functions, shifting the tangential receiver functions by a fixed amount in backazimuth, and solving for degree 1 and 2 arrivals in the joint set of receiver functions. It allows determination of delay time (which scales to depth) and orientation of dipping and anisotropic features without waveform modeling. Combining radial and tangential components with a shift in backazimuth fills holes that may otherwise exist in azimuthal event coverage. We validate the method against active source results from the Wind River Thrust fault in Wyoming and against a waveform modeling study targeting deep crustal anisotropy in southern California. We then present initial results across the continental U.S. using Transportable Array data. First-order features are high amplitudes along the West Coast plate boundary and elevated amplitudes in parts of the intermountain West, a transition to low amplitudes in the central U.S. at the Rocky Mountain/Laramide front, and high amplitudes along the Appalachian–Ouachita belt. Foliation strike roughly aligns with the strike of mountains, but high signal amplitudes and matching strikes outline geological features with little current expression in surface topography, such as the Southern Oklahoma aulacogen, high-grade rocks in the Appalachian Piedmont, and the Midcontinent Rift. We conclude that lithospheric deformation can be targeted with receiver functions without extensive waveform modeling, allowing first cuts through large data sets such as that from USArray.

1. Introduction

The baseline Earth model in seismology is typically 1-dimensional (flat or spherical interfaces) and isotropic. In such a system, seismic wave propagation is decoupled between P–SV waves (oscillating within the vertical plane between source and receiver) and SH waves (oscillating in the plane orthogonal to P–SV). Decoupling

* Corresponding author at: Department of Geological Sciences, University of Colorado Boulder, Boulder, CO 80309-0399, USA
E-mail addresses: vera.schulte-pelkum@colorado.edu (V. Schulte-Pelkum), kevin.mahan@colorado.edu (K.H. Mahan).

http://dx.doi.org/10.1016/j.epsl.2014.01.050
0012-821X/

between P–SV and SH breaks down when seismic anisotropy is present, or when the model is not flat-layered (in a regional approximation; more accurately, not spherically layered). Anisotropy has garnered attention as a means to access a record of past deformation with seismic observables, since ductile deformation leads to preferential mineral alignment. In the lithospheric mantle and in the crust, the resulting anisotropy can be formed at depth and remain preserved, generating a record of past deformation. Most seismic methods that target anisotropy focus on azimuthal anisotropy (i.e. anisotropy with a horizontal symmetry axis) for simplicity of theoretical treatment and easier distinction from isotropic heterogeneity; examples are shear-wave splitting and anisotropic travel time tomography. In surface wave anisotropic studies, azimuthal and radial anisotropy are typically treated separately; azimuthal anisotropy is measured using the variation of phase velocities with backazimuth (e.g. Lin et al., 2011), while radial anisotropy is derived from the phase velocity difference between Rayleigh waves (sampling V_{SV}) and Love waves (sampling V_{SH}; e.g. Moschetti et al., 2010). However, anisotropy does cause Love-to-Rayleigh scattering ("quasi-Love" waves; Park and Levin, 2002), with exceptionally strong coupling for plunging symmetry axis anisotropy (Rieger and Park, 2012; Rieger and Park, submitted for publication).

P–SV to SH decoupling is typically assumed when analyzing receiver functions. The receiver function technique isolates mode conversions of teleseismic waves (most typically P converting to S) at interfaces close to the recording station (Phinney, 1964; Langston, 1977; Vinnik, 1977). In order to find the converted pulses within a complicated P coda that includes a finite source time function and source-side scattering, the vertical component seismogram is taken as a proxy for the source function and deconvolved from the horizontal components; an alternative option is to use the longitudinal particle motion as a proxy for the source and deconvolve from the ray-perpendicular components. In the isotropic, flat-layered case, the tangential component receiver function is zero (or in practice, contains incoherent noise), and the radial component receiver function has backazimuth-independent arrivals that are used to image subsurface interfaces. Actual seismograms show that coherent and azimuthally varying arrivals are often observed on radial as well as tangential component receiver functions, indicating a breakdown of P–SH to SV decoupling and the presence of 2- or 3-dimensional heterogeneity or anisotropy.

Azimuthal (i.e. horizontal symmetry axis) anisotropy leads to a characteristic degree-2 (180°-periodic) backazimuthal pattern in travel times (e.g. Schulte-Pelkum and Blackman, 2003; Lin et al., 2011) as well as receiver functions (Levin and Park, 1997; Savage, 1998). This periodicity is considered diagnostic for anisotropy (e.g. Liu and Niu, 2012), as opposed to the degree-1 (360°-periodic) signal from a velocity contrast across a dipping isotropic interface. However, plunging axis P anisotropy also generates a degree-1 signal (Levin and Park, 1997; Savage, 1998) that has been exploited to map plunging axis anisotropy as well as dipping isotropic interfaces (e.g. Bianchi et al., 2008, 2010). We demonstrate characteristics of radial and tangential component receiver function arrivals from dipping and anisotropic structures, in particular a systematic relationship of the out-of-plane signal between the two components. We introduce a simple technique to map the strike and depth of dipping interfaces or foliation that exploits this relationship without requiring waveform modeling. We recover a known structure (Wind River Thrust) and show agreement with results from a waveform modeling approach in Southern California, followed by continent-wide results from USArray.

2. Method

2.1. Receiver function sensitivity

Levin and Park (1998) demonstrated the effects of P and S anisotropy on teleseismic converted waves in flat-layered media with arbitrarily oriented anisotropy. Our focus is on signals that are generated by inclined or anisotropic structures and are sufficiently large to dominate receiver function appearance (e.g., comparable in amplitude to common used signals such as the conversion from the Moho); we show that these signals can be used to map the presence, the strike, and the depth of dipping and anisotropic structures. We use a ray-based code that handles dipping interfaces and arbitrary anisotropy (Frederiksen and Bostock, 2000) to calculate synthetic seismograms. Results were benchmarked against an isotropic (Randall, 1994) and an anisotropic reflectivity code (Becker et al., 2006) for the flat-layered cases.

2.1.1. Dipping isotropic interface

The first example model has a dipping intracrustal isotropic velocity contrast with $\Delta Vs = 0.3$ km/s. Contrasts in Vp do not affect the conversion amplitude, and a pure Vp contrast with no Vs contrast generates no P–S conversion; a pure Vp/Vs contrast with constant Vs is therefore invisible to receiver functions. This lack of effect of contrast in $(Vp/Vs)_{\delta Vs=0}$ on conversion amplitude is not to be confused with the effect of Vp/Vs of the medium between converter and receiver on the delay time of the arrival, which is significant when converting delay time to depth. The conversion from the dipping intracrustal interface is seen near 2 s delay time in Figs. 1a and 1b. A conversion from a flat interface with a Moho-sized Vs contrast is also shown for comparison and appears at 4.5 s (Fig. 1). Radial and tangential component arrivals from the dipping interface have a 360° periodicity, with a 90° phase offset in backazimuth between the components. The intracrustal conversion reaches a maximum at incidence from the downdip direction, since a shallower angle between incident P and the converting interface causes a larger S conversion, with an amplitude in this model comparable to that of the Moho arrival. We subtract the azimuthal average at each time point (representing the isotropic flat-layered structure) from the radial component. The remaining out-of-plane portion of the radial component (Fig. 1c) is nearly identical to the tangential component modulo a 90° phase shift and some pulse broadening in the corrected radial component due to subtle timing differences between the updip and downdip direction that affect the removal of the azimuthal average. The similarity between corrected components will be exploited for the mapping method in Section 2.2. Note also the zero-delay time, polarity-reversed arrival on the tangential component (Fig. 1b) due to bending of the direct P arrival out of the P–SV plane, a characteristic signature of dipping isotropic interfaces that we will use to make a distinction with plunging axis anisotropy.

Fig. 1d shows the tangential component after a shift of 90° in backazimuth, now matching the out-of-plane radial signal in Fig. 1c. The polarity nodes in the original tangential component (Fig. 1b) appear at the up- and downdip backazimuths. Note that we use a conventional left-handed $R–T–Z$ coordinate system throughout ($+T$ is 90° clockwise from $+R$); the polarity of the tangential component would be reversed in a right-handed system such as used by Levin and Park (1998), resulting in an opposite-sense offset between the corrected radial compared to the tangential components. The nodes in both components are now aligned with the strike orientation, and the two components are nearly identical except for the effect of slight time shifts on the removal of the average signal in the radial component. Both components' polarities would be flipped if the dipping interface had

Please cite this article in press as: Schulte-Pelkum, V., Mahan, K.H. A method for mapping crustal deformation and anisotropy with receiver functions and first results from USArray. Earth Planet. Sci. Lett. (2014), http://dx.doi.org/10.1016/j.epsl.2014.01.050

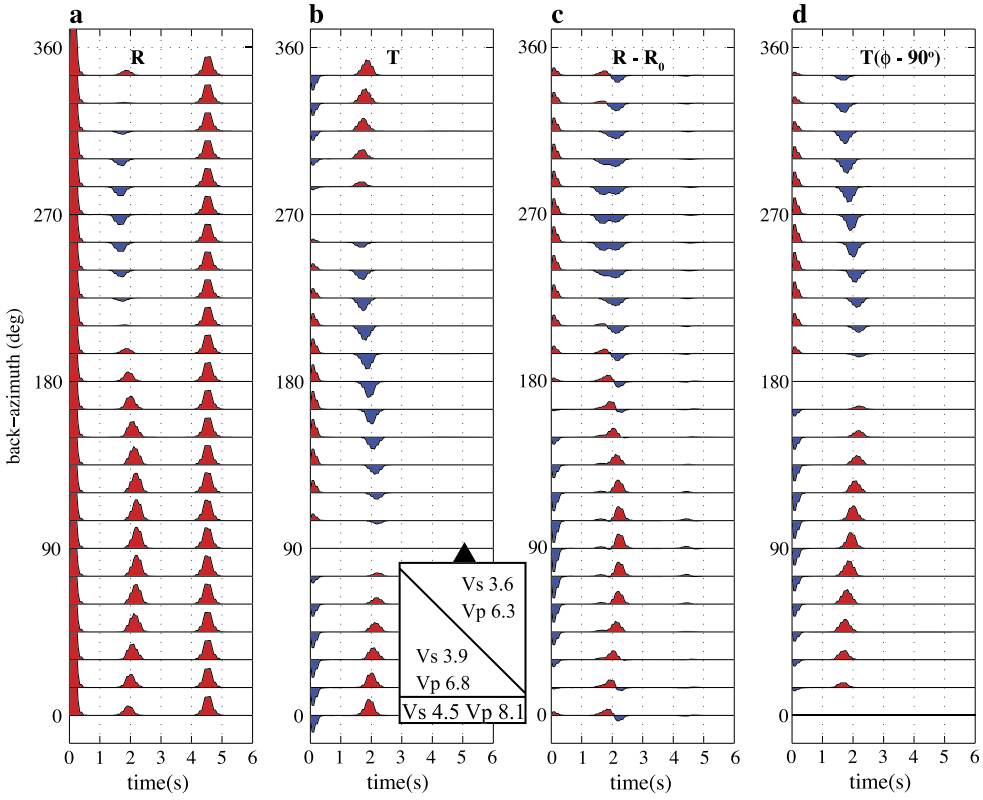

Fig. 1. (a) Radial component synthetic seismograms for a model with a dipping (45° down to E) isotropic interface striking N–S above a flat Moho (see inset; velocities in km/s) as a function of backazimuth. Direct P arrival is at 0 s. Delay times were corrected for incidence angle, so that the corrected time corresponds to vertical incidence. (b) Same as (a), but tangential component. (c) Radial component after azimuthal average was subtracted. (d) Tangential component after shifting by +90° in backazimuth (note that shifting the traces by +90° corresponds to shifting the coordinate system by −90°; hence the notation $T(\phi - 90°)$). Nodes on both components are now in strike orientation, and corrected radial and transverse look similar. The amplitude scale is the same for all panels.

a velocity decrease with depth (fast-over-slow), rather than an increase (slow-over-fast) as shown here. A different dip angle or a different velocity contrast results in a change of the amplitude of the degree-1 pattern. However, the node alignment with strike and the correspondence between the corrected components remain the same.

2.1.2. Anisotropic layer with plunging symmetry axis

The following examples (Figs. 2, 3) show the same treatment as above for synthetic seismograms from anisotropic models. The models contain a 10 km thick anisotropic layer with 6% peak-to-peak hexagonal symmetry anisotropy (inset in Figs. 2, 3; there is no isotropic velocity contrast). Anisotropy of a few percent in bulk deformed crustal rocks is deemed to be a typical strength (e.g., Ji and Salisbury, 1993; Tatham et al., 2008; Ward et al., 2012), although values of over 20% can be seen in some samples (e.g., Godfrey et al., 2000; Lloyd et al., 2009). Mantle anisotropy is usually approximated as having a hexagonal symmetry with a fast symmetry axis, matching the symmetry resulting from predominant olivine with aligned *a*-axes while *b*- and *c*-axes are distributed within a plane perpendicular to them and with the possible addition of orthopyroxene (enstatite; Blackman et al., 2002; Schulte-Pelkum and Blackman, 2003; Becker et al., 2006). In contrast, deep crustal anisotropy is assumed to be dominated by mica (e.g. Erdman et al., 2013; Lloyd et al., 2009; Babuska and Cara, 1991) and is thus approximated as slow-symmetry axis hexagonal (Levin and Park, 1998; Sherrington et al., 2004). However, quartz and amphibole (Ji et al., 2013; Ward et al., 2012; Tatham et al., 2008) also contribute to crustal anisotropy and display fast axis symmetry. We consider both cases in our modeling. We use the converted arrivals generated by contrasts in anisotropy; splitting of converted phases, although used in some studies (Nagaya et al., 2011; Peng and Humphreys, 1997; McNamara and Owens, 1993) is difficult to isolate in receiver functions (Levin and Park, 1997; Savage, 1998) and is not a target in this study.

Hexagonal anisotropy is defined by a symmetry axis and a plane orthogonal to it with constant phase velocities within the plane. The phase velocity surfaces between the symmetry axis and the symmetry plane can take various shapes; one way to express this variation is through the shape factor η. Approaches to handling the shape factor vary, with some workers fixing it to pure ellipsoidal anisotropy (e.g. Levin and Park, 1997, 1998; Ozacar and Zandt, 2009; Sherrington et al., 2004; Porter et al., 2011), which scales the shape factor with the strength of anisotropy along the symmetry axis (Porter et al., 2011). A brief survey of published elasticity tensors for crustal samples (Barruol and Kern, 1996; Godfrey et al., 2000; Tatham et al., 2008; Ward et al., 2012; tensor decomposition by Browaeys and Chevrot, 2004 used to calculate the hexagonal approximation for full tensors, available as part of the *fstrack* package, Becker et al., 2006) shows a range of values of ∼0.4 to less than 1.1 for the shape factor, not always correlated with strength of symmetry axis anisotropy, with mafic samples falling into the higher end of the range. We model anisotropy across this range of values and exploit features that are independent of shape factor and fast vs. slow symmetry axis.

The first example is for a slow axis of symmetry with a horizontal (Fig. 2a) and plunging (Fig. 2b) symmetry axis and a midrange shape factor of 0.7. Conversions with opposite polarities are seen from the top and bottom of the anisotropic layer. The dominant periodicity of the converted arrival changes from 180° in the horizontal symmetry axis case to 360° for the plunging symmetry axis. The dominantly degree-1, large-amplitude arrivals for the plunging symmetry axis case are controlled by Vp anisotropy;

Please cite this article in press as: Schulte-Pelkum, V., Mahan, K.H. A method for mapping crustal deformation and anisotropy with receiver functions and first results from USArray. Earth Planet. Sci. Lett. (2014), http://dx.doi.org/10.1016/j.epsl.2014.01.050

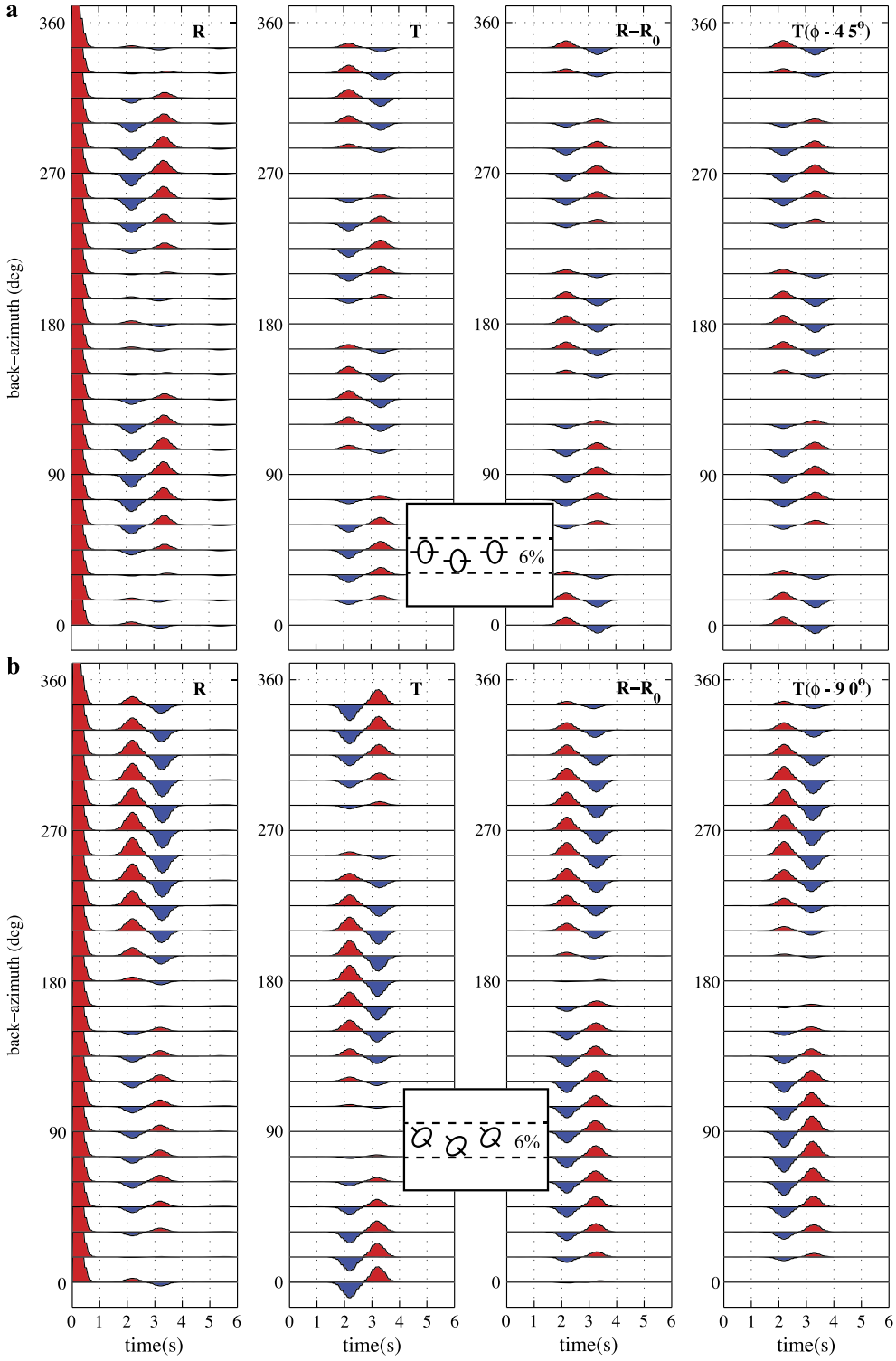

Fig. 2. (a) Synthetic seismograms for a model with an anisotropic layer (from 20 to 30 km depth; see inset) with a horizontal slow symmetry axis, hexagonal symmetry. The symmetry axis orientation is E–W and the Vp and Vs anisotropy amplitude is 6% (defined as $2(v_{max} - v_{min})/(v_{max} + v_{min})$, i.e. % peak-to-peak anisotropy). There is no isotropic velocity contrast. Amplitude scale is the same between all panels in this figure and Fig. 1. R is radial component, T is tangential component, $R - R_0$ is radial component but with azimuthal average removed at every time step as in Fig. 1c, $T(\phi - 45°)$ is tangential component shifted by +45°. Note the similarity between the latter two. (b) Synthetic seismograms for same model, except symmetry axis plunging 45° down from horizontal to E (90° backazimuth; see inset). Components are as above, except azimuthal shift for tangential component is now 90°.

pure Vp anisotropy with no Vs anisotropy (a theoretical construct) produces nearly identical synthetic seismograms to the case with Vp and Vs anisotropy, while pure Vs anisotropy shows degree-2 arrivals even for a plunging symmetry axis (Levin and Park, 1998) that are small except for small values of η. Note the contrast to the isotropic interface case, where Vp contrast is irrelevant and the Vs contrast determines the conversion amplitude. The conversion amplitude for the anisotropic plunging symmetry axis case trades off with the strength of anisotropy and is influenced by the shape factor.

The right panels of Figs. 2a and 2b show the radial component after subtracting the azimuthal average at each time step and the

Please cite this article in press as: Schulte-Pelkum, V., Mahan, K.H. A method for mapping crustal deformation and anisotropy with receiver functions and first results from USArray. Earth Planet. Sci. Lett. (2014), http://dx.doi.org/10.1016/j.epsl.2014.01.050

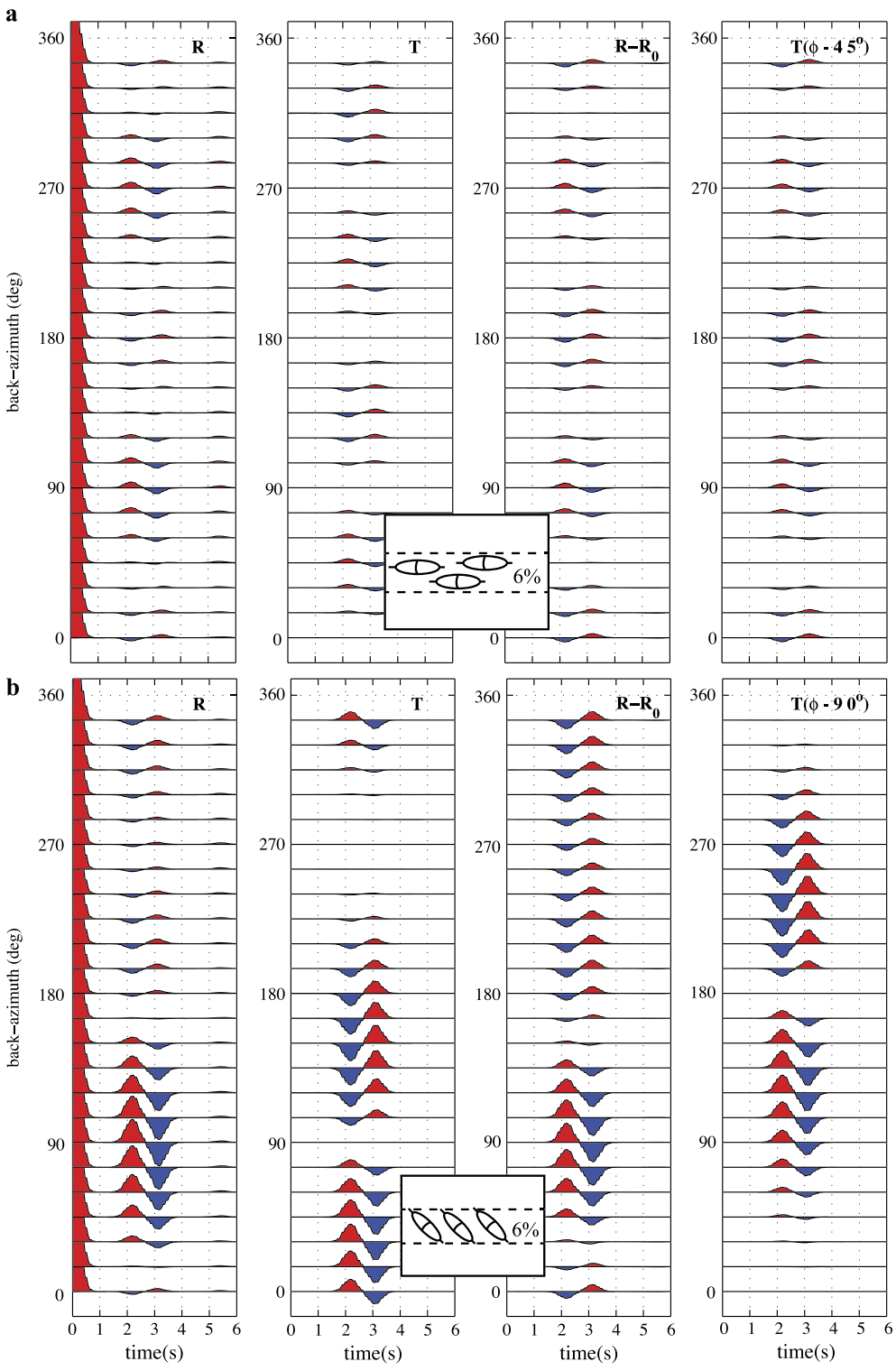

Fig. 3. Same as for Fig. 2, except with a fast rather than slow symmetry axis.

tangential component after shifting it by 45° in backazimuth for the horizontal symmetry axis case and by 90° in the plunging symmetry axis case. As in the case for the dipping isotropic interface in Fig. 1, the corrected components show a near perfect match, again with nodes along the strike orientation. The strike is that of the foliation plane, the plane perpendicular to the slow symmetry axis. A crucial difference to the isotropic dipping interface case is the lack of a direct P arrival on the corrected radial and on the tangential component.

The second example is for a fast symmetry axis and a shape factor of 1.03, approximating olivine-dominated mantle anisotropy (Farra et al., 1991) and some mafic crustal materials with lineation, with the lineation identifying the fast symmetry axis (Tatham et al., 2008; Ji et al., 2013). Modeling is again performed for a horizontal (Fig. 3a) and plunging (Fig. 3b) symmetry axis. Amplitudes for the horizontal symmetry axis case are small, an observation that holds for the entire range of η considered here for fast horizontal symmetry axes, as well as for the higher range of η for

Please cite this article in press as: Schulte-Pelkum, V., Mahan, K.H. A method for mapping crustal deformation and anisotropy with receiver functions and first results from USArray. Earth Planet. Sci. Lett. (2014), http://dx.doi.org/10.1016/j.epsl.2014.01.050

horizontal slow symmetry axes. The smaller amplitudes observed for horizontal axis (azimuthal) anisotropy compared to plunging axis anisotropy may explain why the majority of receiver function studies appear to recover the latter.

In the plunging symmetry axis case (Fig. 3b), the nodes again align with the strike of the plane perpendicular to the symmetry axis, just as in the slow axis case above. The nodes of the corrected components show slight shifts from the strike orientations due to an influence of a small degree-2 component. The same behavior is seen for very low and very high values of η in the slow symmetry axis case. However, fitting a degree-1 component recovers the strike azimuth correctly within $\pm 10^\circ$ for the entire range of η considered here and within a few degrees in most of the cases. Similar variations occur with varying dip or plunge angles. We exploit the common features observed in the synthetic modeling to develop a method for mapping the strike and depth of dipping foliation and dipping interfaces in Section 2.2.

2.2. Mapping method

Most receiver function studies targeting the crust and subduction zones published to date rely on matching observed receiver functions via waveform modeling to determine anisotropic model parameters (e.g., McCormack et al., 2013; Wirth and Long, 2012; Song and Kim, 2012; Agostinetti et al., 2011; Eckhardt and Rabbel, 2011; Porter et al., 2011; Roselli et al., 2010; Nikulin et al., 2009; Ozacar and Zandt, 2009; Mercier et al., 2008; Levin et al., 2008; Shiomi and Park, 2008; Obrebski and Castro, 2008; Schulte-Pelkum et al., 2005; Sherrington et al., 2004; Zandt et al., 2004; Vergne et al., 2003; Leidig and Zandt, 2003; Levin et al., 2002a, 2002b; Levin and Park, 1997). Besides being computationally intensive, this approach is subject to strong tradeoffs between anisotropic strength, anisotropic geometry, and isotropic structure, and typically requires assumptions about the symmetry and geometry to reduce the number of free parameters (down from 21 elastic constants for general anisotropy, but often constraining even hexagonal anisotropy to fewer than the full 5 parameters as discussed for the choice of shape factor above). Similar tradeoff problems (such as between dip and velocity contrast) are encountered when trying to solve for heterogeneous isotropic structure, e.g. Moho dip (e.g. Hayes and Furlong, 2007; Frederiksen and Bostock, 2000). We seek a simpler method to infer basic parameters without requiring a full model of anisotropy or isotropic heterogeneity, akin to the basic parameters of delay time and fast polarization orientation in shear wave splitting analysis (e.g. Savage, 1999; Park and Levin, 2002; Long and Silver, 2009).

Based on our forward modeling, the robustly observable parameters for each station location are (1) The presence of a dipping isotropic interface or dipping foliation contrast, indicated by the presence of 360°-periodic arrivals with a 90° azimuthal shift between radial and tangential components; (2) The strike of those interfaces, as constrained by polarity nodes; (3) The delay time of that arrival, which scales to depth of the interface. These three parameters can be used in hypothesis testing of geological models without having to fit a detailed anisotropic and/or heterogeneous model for the lithosphere. The simple procedure is as follows: (1) Calculate radial and tangential component receiver functions; (2) Subtract the azimuthal average from each radial component receiver function, and add 90° to the backazimuth of the tangential component receiver functions; (3) Combine the two corrected components and solve for a degree-1 sinusoidal function over backazimuth at each time point; the nodes constrain the interface strike or the strike of the plane perpendicular to the symmetry axis (in the case of slow axis symmetry, the strike of the foliation plane), and the delay time of large amplitude arrivals maps to depth. An isotropic dipping interface can be distinguished from plunging axis anisotropy by the presence of a matching arrival at zero delay time with the same nodes but opposite polarity to that of the later arrival. Azimuthal anisotropy is treated the same, except that the tangential component is shifted by 45° rather than 90° and the nodes constrain the azimuthal orientation of a fast or slow symmetry axis and the axis perpendicular to it (no a priori distinction is required between the two cases).

We deliberately avoid interpreting polarities because of the inherent ambiguity between fast and slow symmetry axes (making a distinction would require assumptions about the material). Another polarity ambiguity is caused by the question of whether a given arrival represents the top or the bottom of an anisotropic layer, since the sharpness of the anisotropic contrast at the top versus bottom may be different and it may not always be possible to see both interfaces. Interpreting the strike does not require solving these ambiguities. We show applications in Section 3.

3. Results

We demonstrate applications of the method for three different cases: An isotropic dipping velocity contrast previously imaged with active source data (the Wind River Thrust fault, Wyoming, USA); a comparison with a previous waveform modeling-based study in Southern California; and results across the continental U.S. from USArray. The receiver function processing in all three cases is as follows. We begin with all events with magnitude $m_b > 5.1$ recorded at epicentral distances from 30–140° (targeting P and P_{diff}) and calculate radial and tangential component receiver functions using the time-domain iterative deconvolution algorithm by Ligorria and Ammon (1999), with a Gaussian filter of 3 (corresponding to a pulse width of 1 s). The inclusion of P_{diff} in the analysis increases event coverage particularly in the Central and Eastern U.S., where southwestern Pacific subduction zones move out of the P distance range.

Receiver functions are retained for analysis if all of the following criteria are fulfilled: The signal-to-noise ratio of the initial vertical component is at least 1.5 (calculated with a noise window of 35 s to 5 s before predicted P, and a signal window of 5 s before to 25 s after predicted P, after applying a bandpass filter from 33 to 0.25 s period); the convolution of the calculated receiver function with the vertical component reproduces the horizontal component to at least 60% (variance reduction as defined in Ligorria and Ammon, 1999); the radial component receiver function shows a positive polarity direct P arrival that is the largest arrival in the receiver function; the receiver function amplitude (representing the horizontal to vertical amplitude ratio, H/Z) does not exceed 2; any arrivals' pulse length does not exceed 3.5 s (the latter two criteria are applied since very high amplitudes and long oscillatory pulses are hallmarks of an unstable deconvolution); and any tangential component receiver function has a radial component receiver function from the same event that passed quality control. After automated sifting, manual spot checks find only a few outliers remaining at each station.

3.1. Local fault imaging

The first example is a test of the method on a known dipping isotropic structure, the Wind River Thrust fault in Wyoming in the U.S. (Fig. 4a). Active source imaging showed a steeply (30–48° from horizontal) dipping fault to ~20 km depth in the southern part of the range, including a basement-over-sediment overthrust to ~12 km depth (Smithson et al., 1979; Stone, 1987; Steidtmann and Middleton, 1991; Fig. 4b). Two permanent broadband stations are nearly collocated at 60 m distance to each other (BW06 and PD31) about 60 km NW of the active source pro-

Please cite this article in press as: Schulte-Pelkum, V., Mahan, K.H. A method for mapping crustal deformation and anisotropy with receiver functions and first results from USArray. Earth Planet. Sci. Lett. (2014), http://dx.doi.org/10.1016/j.epsl.2014.01.050

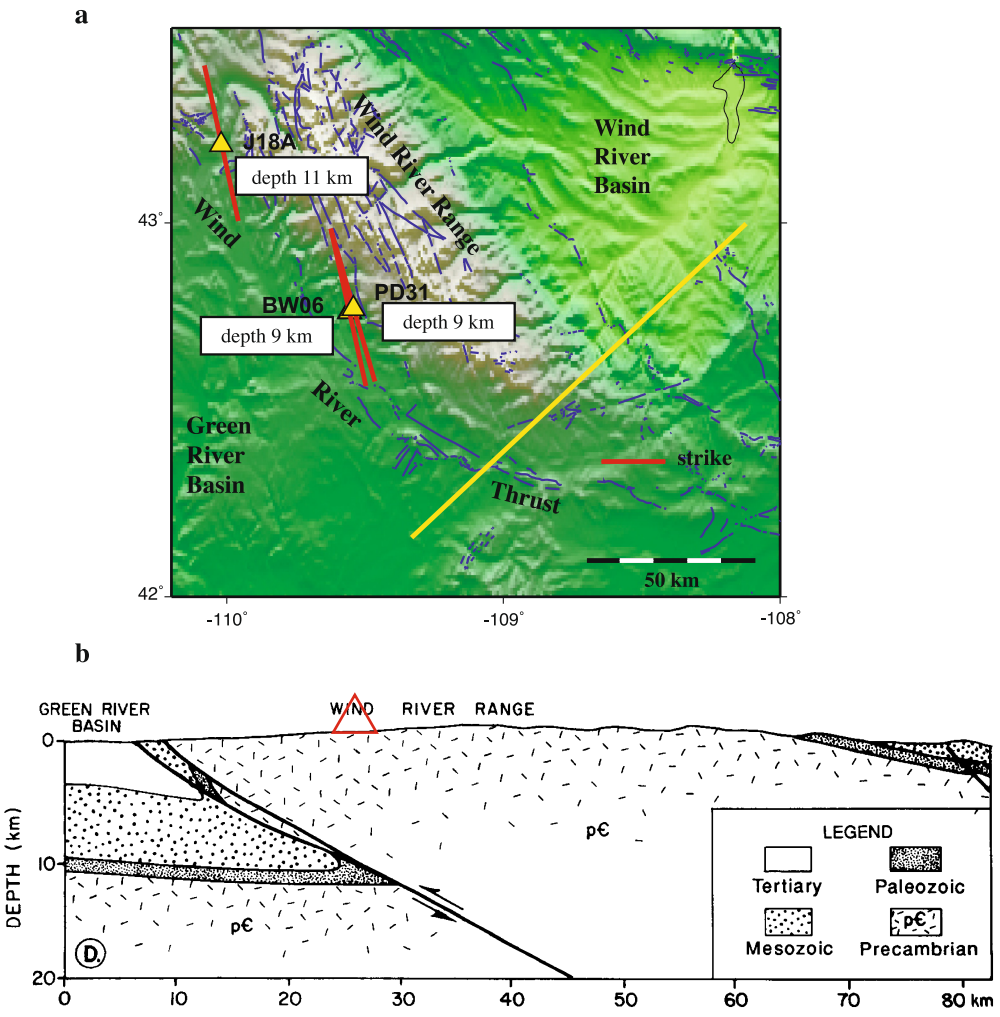

Fig. 4. (a) Topographic map of the Wind River Range and surroundings. Faults from USGS database in blue. Approximate location of COCORP active source line (Smithson et al., 1979) in yellow. Stations J18A, BW06, and PD31 shown as yellow triangles (symbol for PD31 was minimally shifted for visibility). Red bars are strike orientation of the highest amplitude degree-1 arrival. Depth to the dipping interface calculated from the delay time of the same arrival is shown in a white box for each station. (b) One interpretation of the COCORP seismic line, showing the basement-over-sediment overthrust and the approximate location (red triangle) of the stations shown in (a) on the section. Adapted from Steidtmann and Middleton (1991) after Stone (1987).

file. An EarthScope Transportable Array station (J18A) sits another 62 km to the NW from the other two stations.

While the exact deep geometry of the thrust fault north of the active source profile is unknown and mapping of the branches of the Wind River Thrust varies (Blackstone, 1993; De Vries et al., 1990), basement-over-sediment overthrusts are inferred along the range, merging into another crystalline overthrust along the Gros Ventre Range to the NW. All three stations likely sit atop the overthrust (Fig. 4). We calculated radial and tangential component receiver functions for the three stations and applied time and amplitude corrections for incident slowness (Jones and Phinney, 1998). After subtraction of the azimuthal average from the radial component, and after applying the 90° azimuthal shift to the tangential component, all three stations show characteristic arrivals between 1.2–1.5 s that are very similar between the two components (Fig. 5 and Figs. S1, S2 in the supplementary information) indicating a dipping interface with NNW-SSE strike at roughly 10 km depth, and a polarity-reversed zero delay arrival suggesting a dipping isotropic shear velocity contrast at depth (rather than anisotropy). Fig. 5 shows azimuthally binned plots of the radial component after subtraction of the azimuthal average, the tangential component after shifting by 90° in backazimuth, and the combined components. Fitting an azimuthal degree-1 signal to the combined components at each time step results in a phase and delay time for the maximum degree-1 arrival that match inferred fault depth from the active source results to the SE (see compilation in Steidtmann and Middleton, 1991) and align with mapped faults (Fig. 4).

Stations BW06 and PD31 are collocated with the 11-element short-period vertical component Pinedale array (PDAR; Fig. S3). Array processing shows no significant out-of-plane propagation, supporting the interpretation of the arrivals as bending and conversion from the dipping fault interface, rather than lateral scattering (e.g. Jones and Phinney, 1998; Abers, 1998; Fig. S4).

3.2. Comparison to waveform-fitting-based approach to resolve anisotropy

The second example shows a regional subset of stations in Southern California that were analyzed in a previously published study (Porter et al., 2011) employing a waveform modeling approach to extract information on deep crustal anisotropy from receiver functions.

Porter et al. (2011) used a neighborhood algorithm to fit radial and tangential receiver functions in the 4 seconds preceding the Moho arrival by varying anisotropic layer thickness and depth, % anisotropy, and trend and plunge of the symmetry axis, while prescribing fixed isotropic properties and ellipsoidal hexag-

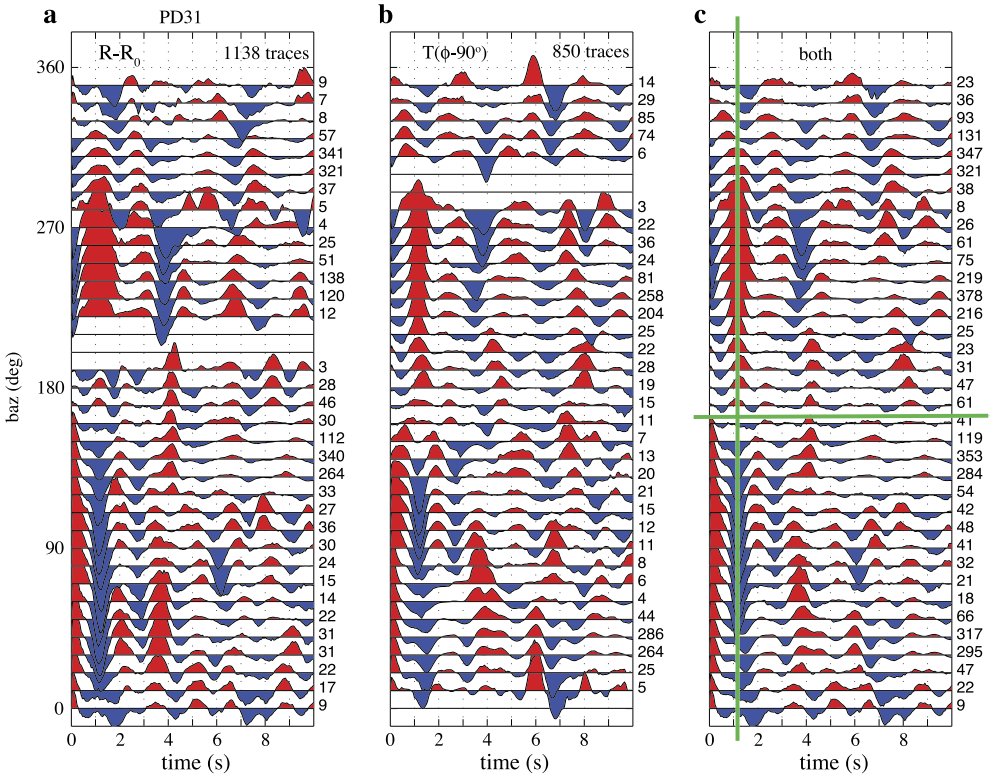

Fig. 5. Receiver functions for station PD31 in Fig. 4. (a) Radial receiver functions after correcting timing to vertical incidence and amplitude for incidence angle and subtracting the azimuthally averaged amplitude at each delay time point, shown binned by backazimuth, with half-bin (5°) smoothing. Number of receiver functions contributing to each bin shown on right of each trace. (b) Tangential receiver functions after incidence angle correction of timing to vertical incidence, with 90° added to backazimuth, binning same as in (a). (c) Corrected radial and tangential component receiver functions from panels (a) and (b) binned together using the same parameters as in (a) and (b). The amplitude scale is the same for all panels. Green lines mark strike orientation (phase +90°) and time of the largest degree-1 arrival from fitting a degree-1 function over backazimuth at each time step. The strike is plotted in Fig. 4a, and the same plots are shown for station BW06 and J18A in Figs. S1 and S2 in the supplementary information.

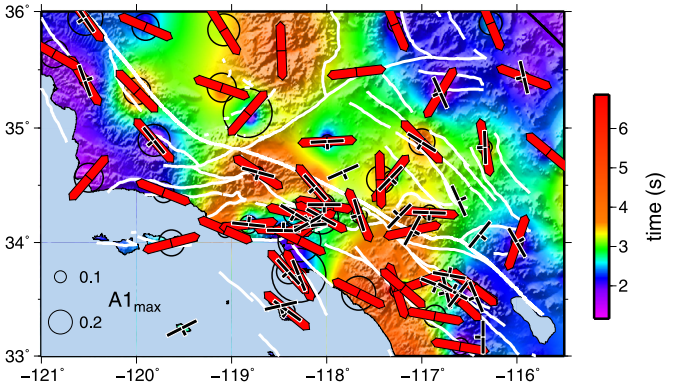

Fig. 6. Comparison of the results from our technique to those from a waveform modeling study (Porter et al., 2011) in Southern California. White lines are fault traces. Red bars are strike of highest amplitude degree-1 arrival between 1–8 s at each station from this study, shown if the arrival exceeds an H/Z amplitude cutoff of 0.05. Color background shows delay time (scaling to depth) of the highest amplitude degree-1 arrival. Circles scale with amplitude of the arrival. Black bars show trend of the anisotropic axis (short bar) and strike (long axis) from Porter et al. (2011). Note the agreement between the strikes from this study and Porter et al. (2011).

onal slow-axis symmetry. We use the degree-1 signal amplitude and phase obtained from the corrected radial and tangential components to map strike and delay time as described above. Fig. 6 shows a comparison of symmetry axis-perpendicular strikes (foliation strike when assuming slow axis symmetry) obtained by Porter et al. (2011) and our method. The strike orientations agree well, with less scatter from our method in some areas, and they show alignment with nearby fault orientations. Delay times of the conversions with the largest degree-1 signal in the central region displayed in Fig. 6 are 2.5 s and larger (green–yellow–orange areas in Fig. 6; roughly 20 km and deeper), comparing well to the mid-to lower crustal depths of the Porter et al. (2011) solutions. The comparison leads us to conclude that we can determine strike perpendicular to the anisotropic symmetry axis and delay time of the anisotropic contrast without waveform modeling and without assumptions on the nature of the anisotropy.

3.3. Transportable Array mapping

We analyzed receiver functions for TA stations and stations from the supplementing CI, US, and BK networks with event selection and quality control as described in the beginning of Section 3. TA data were analyzed from 2004 through the end of November 2013, when the array had reached the East Coast but had not recorded there long. Starting with over 2 million calculated receiver functions (counting radial and tangential receiver functions separately), the automated quality control described above retains a median of 13% of traces at each station. The azimuthally invariant portion of the radial signal was used previously in joint inversions with surface waves (Shen et al., 2013a, 2013b, 2013c); here, we target the degree-1 and degree-2 portions that were stripped out for the joint inversion. We solve for degree-1 and degree-2 amplitude and azimuthal phase at each time step, using the resulting degree-1 parameters for the plunging axis case (where the tangential component was shifted by 90°) and the degree-2 solutions for the azimuthal anisotropy case (where the tangential component was shifted by 45°). At each station, we require a minimum of 3 receiver functions per 10° azimuthal bin and a maximum azimuthal gap of less than 90° after combining the corrected radial and tangential components in order to accept a harmonic fit solution. These requirements leave a total of somewhat under 300,000

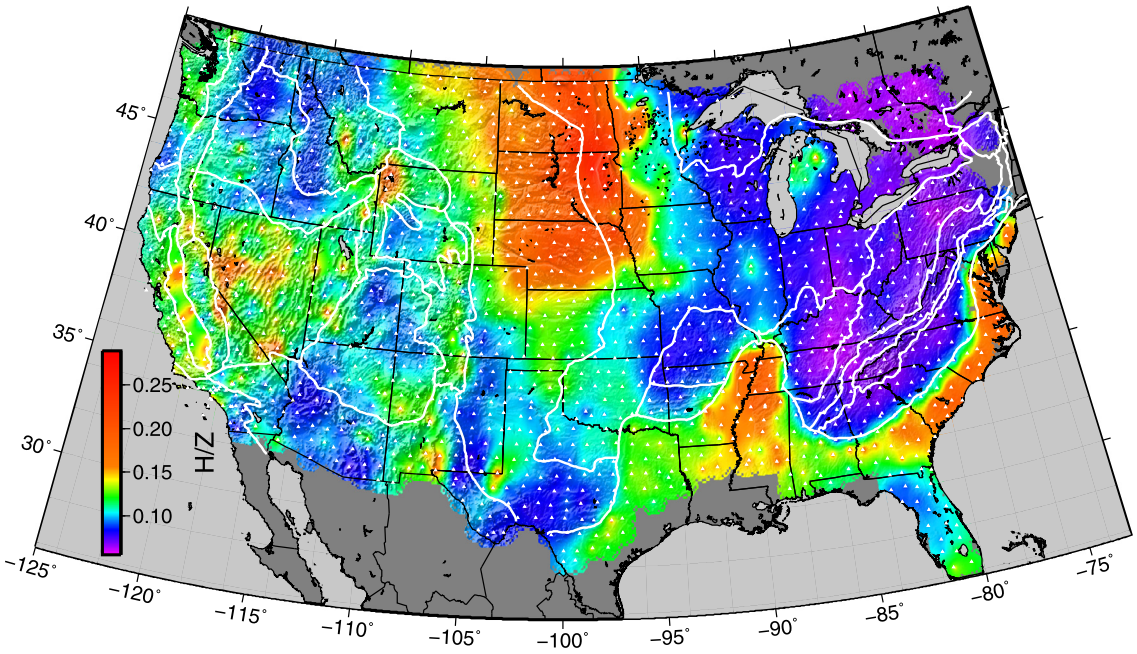

Fig. 7. Map of total signal amplitude in average receiver function at each station from 0–8 s, measured for uncorrected radial and tangential components together. Color scale is H/Z amplitude ratio (with topographic shading superimposed). White triangles show station locations; values were interpolated with tension splines between stations such that the stations lie at extrema. Interpolation is masked for areas farther than 70 km from the closest station. White lines are physiographic province boundaries from Fenneman and Johnson (1946).

receiver functions at 1689 stations producing results in the azimuthal analysis.

Fig. 7 is a map of the average 0–8 s total signal amplitude per receiver function at each station, a time range that spans conversions from the crust including the Moho. Low-velocity unconsolidated sediments amplify receiver function arrivals because of refraction to near-vertical incidence angles, large conversions from the contrast at the interface, and reverberations within the layer (e.g. Langston, 2011). Aside from local and regional signals, obvious large-scale patterns in Fig. 7 are large amplitudes across North and South Dakota and Nebraska, terminating near the border to Kansas where Cretaceous sediments give way to older cover (Reed et al., 2005); in the Mississippi Embayment (thick sedimentary cover extends to the Gulf Coast, where many stations did not pass the automated quality control as applied in this analysis because of large sediment conversion and reverberation amplitudes); and along the Atlantic coastal plain, terminated in the south by the Florida carbonate platform.

We perform a degree-1 fit with a 90° tangential component azimuthal shift and a degree-2 fit with 45° shift at each time step from 0–8 s delay time. Fig. 8 shows degree-1 amplitudes at each station averaged from 0–8 s, normalized by the total average receiver function amplitude in the same time window. Also plotted are strikes from the largest degree-1 arrival at a station if the degree-1 amplitude of that arrival exceeds a threshold value (an H/Z ratio of 0.15). On a continental scale, first-order features in the degree-1 signal are high amplitudes along the West Coast plate boundary, elevated amplitudes in parts of the intermountain West, a transition to low amplitudes in the central U.S. at the Rocky Mountain/Laramide front, and high amplitudes along the Appalachian–Ouachita belt. A comparison to the total amplitude map in Fig. 7 shows that the degree-1 signal amplitude is not simply dominated by geographical patterns in the total signal amplitude used for normalization at each station (for instance, the entire central U.S. shows low degree-1 amplitudes despite the north–south dichotomy in total signal amplitude).

On a large scale, strikes in areas with high average degree-1 amplitudes (Fig. 8) are roughly subparallel to the western plate boundary, the Laramide front, and the Proterozoic Grenville and Paleozoic Appalachian–Ouachita belts. Regional scatter is at least partly due to actual regional scale variations that are not decipherable on a continental scale map, as seen in the Southern California example (compare Fig. 8 to Fig. 6). Similar geographical patterns in amplitude and orientation appear in the azimuthal anisotropy represented by the degree-2 solution (Fig. S7). Because of the ambiguity between the orientation of the fast axis/slow plane or slow axis/fast plane, the azimuthal (horizontal symmetry axis) anisotropy is more difficult to interpret on a continental scale and we do not discuss it further in this paper.

The presence of a direct P arrival at zero delay time with opposite phase compared to a later arrival phase (same node positions and opposite polarity; Fig. 1) should be diagnostic of an isotropic dipping converter, as opposed to a contrast with plunging axis anisotropy. Figs. S5 and S6 show examples of stations with likely anisotropic degree-1 signals (a large-amplitude midcrustal arrival with no matching zero delay arrival). We attempt to make this distinction for the large-amplitude degree-1 arrivals across the network by testing for degree-1 signals in the first 0.25 s with an azimuthal phase that lies within ±20° of the opposite azimuth to the phase of a later large-amplitude arrival. Results are shown in Fig. 9, with isotropic dipping signals shown in red, signal from plunging axis anisotropy in blue, and delay time (scaling to depth within the crust) of the later arrival shown as background shading. While there are some local concentrations of dipping interface arrivals, the results appear dominated by anisotropy. The test may be confounded by delayed direct P arrivals at stations on sedimentary cover; a more accurate test would require identifying the direct P arrival time and adjusting the time windows used for direct vs. converted arrivals at each station. Alignment of dipping interface strike with the strike of foliation (or the strike of the plane perpendicular to plunging lineation) is expected if interface dip and foliation were developed in the same deformation process, for instance retrograde reactions that lead to growth and alignment of mica in a shear zone, generating anisotropy and a simultaneous change in the isotropic bulk wavespeed within the shear zone; foliation strike and strike of the shear zone would be expected to be

Please cite this article in press as: Schulte-Pelkum, V., Mahan, K.H. A method for mapping crustal deformation and anisotropy with receiver functions and first results from USArray. Earth Planet. Sci. Lett. (2014), http://dx.doi.org/10.1016/j.epsl.2014.01.050

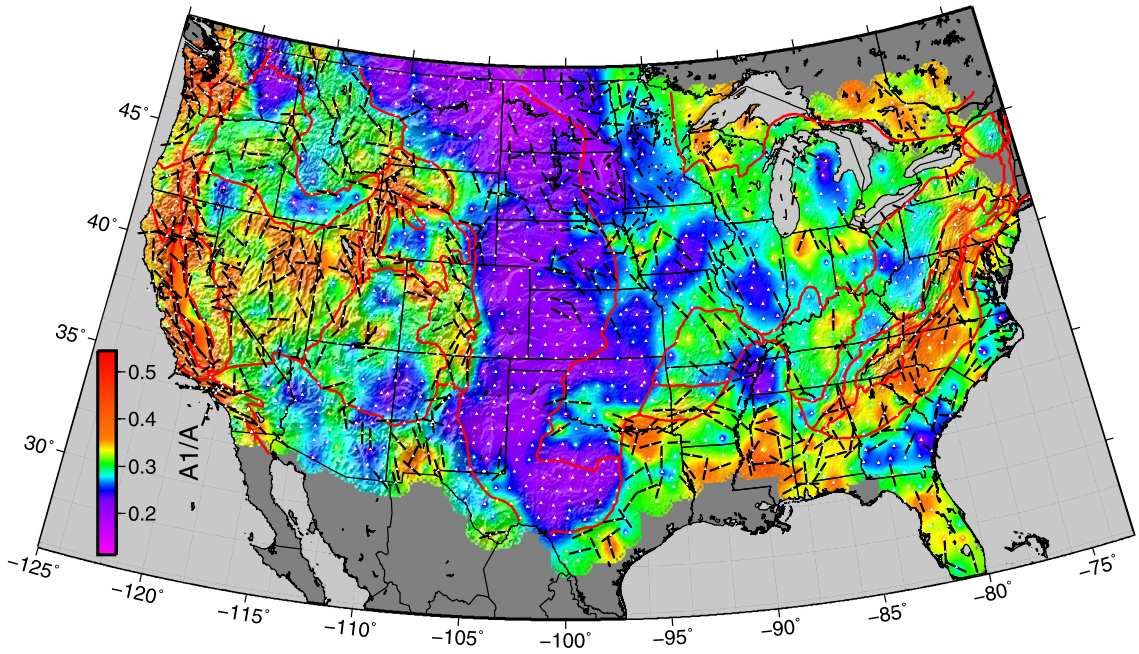

Fig. 8. As in Fig. 7, but background color shows degree-1 signal amplitude (in corrected radial and tangential receiver functions averaged from 0–8 s, interpreted as isotropic dip or plunging axis anisotropy averaged through the crust and Moho) as fraction of the total signal amplitude shown in Fig. 7. Black bars show strike for the highest amplitude degree-1 arrival at each station, plotted if the arrival amplitude exceeds an H/Z ratio of 0.15. The strike represents that of an isotropic dipping interface or of the plane perpendicular to a plunging symmetry axis (foliation strike in the case of a slow symmetry axis).

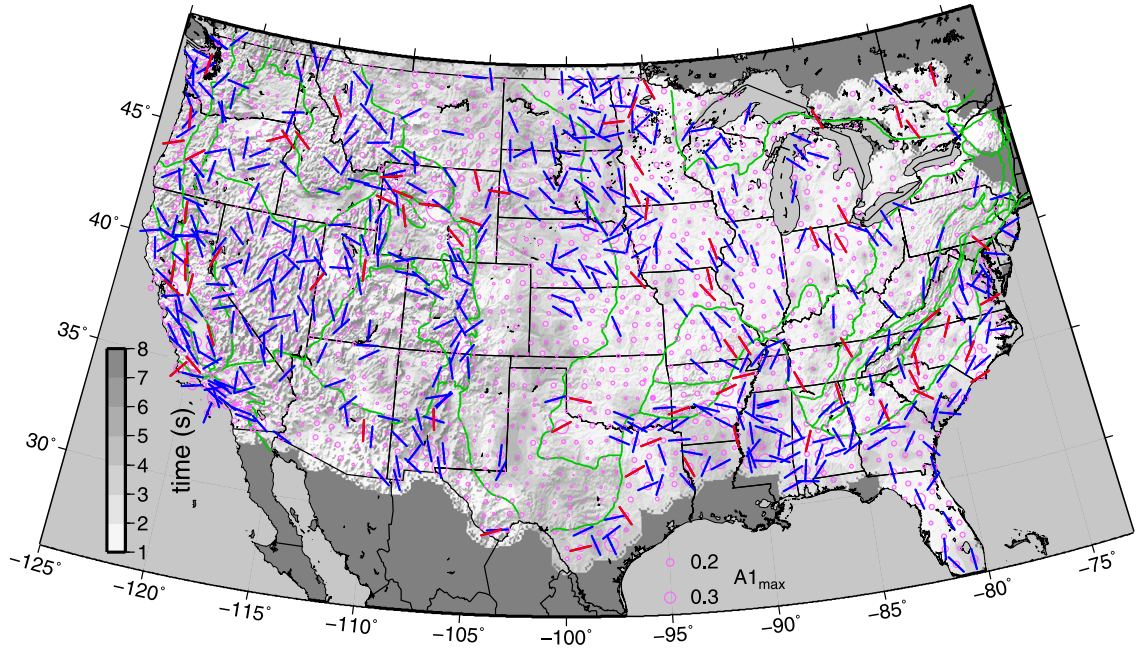

Fig. 9. Map of delay time of largest degree-1 arrival occurring between 1–8 s in greyshade (light = shallower, dark = deep, 1 s corresponding to ~8–9 km depth depending on P and S velocity above the converter), overlaid with topographic shading. Pink circles scale with amplitude of the arrival. Red bars are strikes for arrivals exceeding 0.15 H/Z ratio that show an opposite phase direct P arrival, indicating an isotropic dipping interface. Blue bars show the same but without a matching direct P arrival, indicating plunging axis anisotropy.

related. A similar relationship may be observed in shales deformed near a fault with an isotropic contrast due to fault offset.

Fig. 10 shows the same map as Fig. 8 (degree-1 signal amplitude averaged through the crustal thickness and maximum arrival strikes) with geological elements overlaid. The high signal amplitudes west of the Rocky Mountain Front show an excursion to the east from the physiographic province boundary to include the Black Hills (marked with B in Fig. 10) in South Dakota, correctly identifying the Laramide deformation front. In the central U.S., the NW–SE strikes we infer transect the generally NE–SW orientation of the Yavapai (Fig. 10, Yv) and Mazatzal (Mz) province boundaries (e.g., Whitmeyer and Karlstrom, 2007), suggesting that development of any associated structures post-date the earliest phases of Proterozoic continental assembly. However, there are hints of correlations of regions with elevated degree-1 amplitude with Middle (Midcontinent Rift, M) and Late Proterozoic

Please cite this article in press as: Schulte-Pelkum, V., Mahan, K.H. A method for mapping crustal deformation and anisotropy with receiver functions and first results from USArray. Earth Planet. Sci. Lett. (2014), http://dx.doi.org/10.1016/j.epsl.2014.01.050

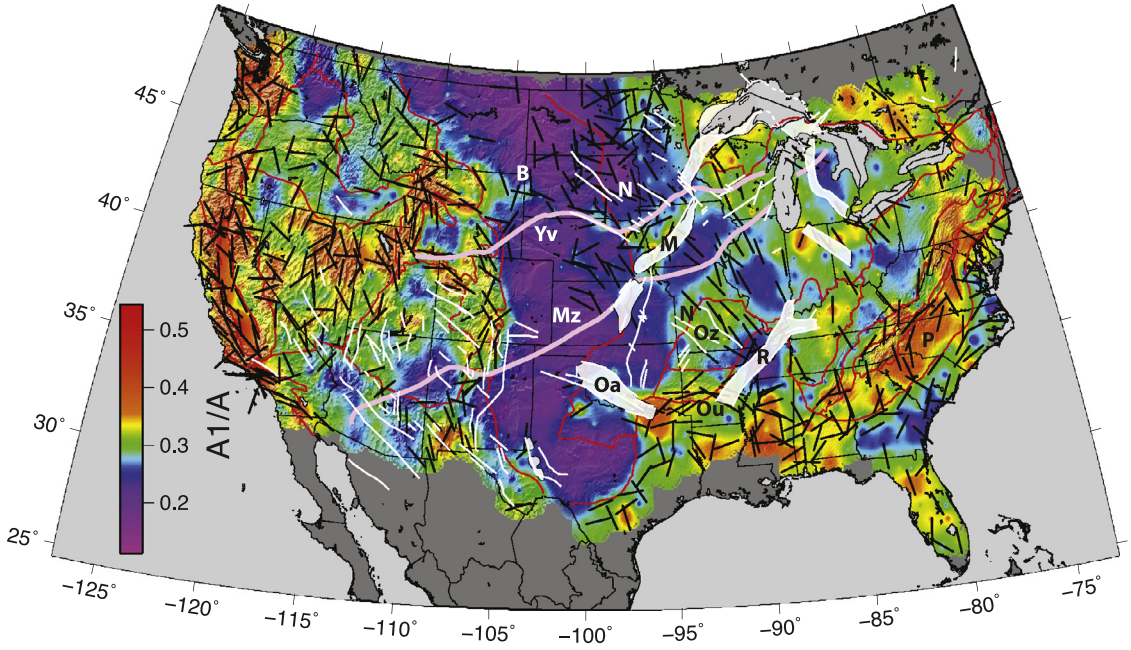

Fig. 10. Same as Fig. 8 with geological elements (Whitmeyer and Karlstrom, 2007) overlaid. B – Black Hills; N – normal faults (white lines); Yv – Yavapai and Mz – Mazatzal (pink lines); M – Midcontinent Rift; Oz – Ozark Plateau; Oa – Southern Oklahoma aulacogen; Ou – Ouachita Belt; R – Reelfoot Rift; P – Appalachian Piedmont.

failed rift systems (Southern Oklahoma aulacogen, Oa). A correlation may exist between mapped NW–SE striking normal faults (N) with elevated degree-1 amplitudes (Ozark Plateau, Oz) and strikes of high-amplitude degree-1 signal in the mid-continent region. High amplitudes and E–W strikes link the Paleozoic Ouachita belt (Ou) to the concurrent Appalachian deformation. While having lower topography and relief than the Blue Ridge and Valley and Ridge provinces to the west, the Appalachian Piedmont (P) has the highest-grade deformed rocks and the strongest degree-1 signal amplitude among the Appalachian provinces. Although these correlations seem plausible, we strongly caution that all station solutions are generated automatically and must be reviewed individually (including estimation of errors based on data coverage, which varies due to noise conditions at each station) before making interpretations on a regional or local scale; particularly east of the Mississippi, event coverage becomes progressively sparser in the currently analyzed data set, and results may change as event coverage improves with recording time. The results presented here are only a first cut intended show that large-scale processing is feasible and that continental-scale features do appear.

4. Conclusions

Waveform modeling approaches can be used to provide a measure of anisotropy and dipping velocity contrasts using receiver functions; however, multiple tradeoffs exist and it is necessary to narrow down parameter space by imposing assumptions on geometry and anisotropy symmetry. We show that large-amplitude azimuthally varying arrivals in receiver functions stem from plunging axis anisotropy and from dipping interfaces, and that these arrivals can be used to isolate fundamental parameters of dipping foliation and interfaces, independently from details such as fast- or slow-symmetry axis anisotropy and other parameters of anisotropic symmetry such as shape factor, exact dip angle, sense of dip, velocity contrast, and anisotropy strength. The tractable parameters are the presence of dipping foliation contrasts or interfaces, their strike, and their depth. These parameters provide useful geological information and allow tectonic hypothesis testing, and can be related to lithospheric deformation across the continental U.S.

Acknowledgements

This material is based upon work supported by the National Science Foundation under Grant Numbers EAR-1251193, EAR-1053291, and EAR-0948581. Waveforms and metadata for TA, US, BK, CI, and IM networks were accessed via the Incorporated Research Institutions for Seismology (IRIS) Data Management System, specifically the IRIS Data Management Center; the IRIS DMS is funded through the National Science Foundation and specifically the GEO Directorate through the Instrumentation and Facilities Program of the National Science Foundation under Cooperative Agreement EAR-1063471. Data from the TA network were made freely available as part of the EarthScope USArray facility, operated by IRIS and supported by the National Science Foundation, under Cooperative Agreements EAR-0323309, EAR-0323311, EAR-0733069. Generic Mapping Tools were used to prepare some figures (Wessel and Smith, 1998). We thank Craig Jones, Weisen Shen, and Francis Wu for discussions. Comments by Maureen Long and two anonymous reviewers substantially improved the paper.

References

Abers, G.A., 1998. Array measurements of phases used in receiver-function calculations: Importance of scattering. Bull. Seismol. Soc. Am. 88, 313–318.
Agostinetti, N.P., Bianchi, I., Amato, A., Chiarabba, C., 2011. Fluid migration in continental subduction: The Northern Apennines case study. Earth Planet. Sci. Lett. 302, 267–278.
Babuska, V., Cara, M., 1991. Seismic Anisotropy in the Earth. Kluwer, Dordrecht.
Barruol, G., Kern, H., 1996. Seismic anisotropy and shear wave splitting in the lower crustal/upper mantle transition (Ivrea Zone). Experimental and calculated data. Phys. Earth Planet. Inter. 95, 175–194.
Becker, T.W., Schulte-Pelkum, V., Blackman, D.K., Kellogg, J.B., O'Connell, R.J., 2006. Mantle flow under the western United States from shear wave splitting. Earth Planet. Sci. Lett. 247, 235–251.
Bianchi, I., Piana Agostinetti, N., de Gori, P., Chiarabba, C., 2008. Deep structure of the Colli Albani volcanic district (central Italy) from receiver function analysis. J. Geophys. Res. 113, B09313. http://dx.doi.org/10.1029/2007JB005548.
Bianchi, I., Park, J., Agostinetti, N.P., Levin, V., 2010. Mapping seismic anisotropy using harmonic decomposition of receiver functions: An application to Northern Apennines, Italy. J. Geophys. Res. 115, B12317.

Please cite this article in press as: Schulte-Pelkum, V., Mahan, K.H. A method for mapping crustal deformation and anisotropy with receiver functions and first results from USArray. Earth Planet. Sci. Lett. (2014), http://dx.doi.org/10.1016/j.epsl.2014.01.050

Blackman, D.K., Wenk, H.R., Kendall, J.M., 2002. Seismic anisotropy of the upper mantle: 1. Factors that affect mineral texture and effective elastic properties. Geochem. Geophys. Geosyst. 3, U1–U24.

Blackstone Jr., D.L., 1993. Precambrian basement map of Wyoming: Outcrop and structural configuration. Geological Survey of Wyoming, Map Series 43.

Browaeys, J.T., Chevrot, S., 2004. Decomposition of the elastic tensor and geophysical applications. Geophys. J. Int. 159, 667–678.

De Vries, J.L., Crockett, F., Sundell, K., 1990. Wyoming centennial field trip featuring Wyoming sedimentation and tectonics. In: 41st Annual Field Conference Road Logs. Wyoming Geological Association.

Eckhardt, C., Rabbel, W., 2011. P-receiver functions of anisotropic continental crust: a hierarchic catalogue of crustal models and azimuthal waveform patterns. Geophys. J. Int. 187, 439–479.

Erdman, M.E., Hacker, B.R., Zandt, G., Seward, G., 2013. Seismic anisotropy of the crust: electron-backscatter diffraction measurements from the Basin and Range. Geophys. J. Int. http://dx.doi.org/10.1093/gji/ggt287.

Farra, V., Vinnik, L.P., Romanowicz, B., Kosarev, G.L., Kind, R., 1991. Inversion of teleseismic S particle motion for azimuthal anisotropy in the upper mantle: a feasibility study. Geophys. J. Int. 106, 421–431.

Fenneman, N.M., Johnson, D.W., 1946. Physical Divisions of the United States. U.S. Geological Survey, Washington, D.C.

Frederiksen, A.W., Bostock, M.G., 2000. Modelling teleseismic waves in dipping anisotropic structures. Geophys. J. Int. 141, 401–412.

Godfrey, N.J., Christensen, N.I., Okaya, D.A., 2000. Anisotropy of schists: Contribution of crustal anisotropy to active source seismic experiments and shear wave splitting observations. J. Geophys. Res. 105, 27,991–28,007. http://dx.doi.org/10.1029/2000JB900286.

Hayes, G.P., Furlong, K., 2007. Abrupt changes in crustal structure beneath the coast ranges of northern California – developing new techniques in receiver function analysis. Geophys. J. Int. 170 (1), 313–336.

Ji, S., Salisbury, M.H., 1993. Shear-wave velocities, anisotropy and splitting in high-grade mylonites. Tectonophysics 221, 453–473.

Ji, S., Shao, T., Michibayashi, K., Long, C., Wang, Q., Kondo, Y., Zhao, W., Wang, H., Salisbury, M., 2013. A new calibration of seismic velocities, anisotropy, fabrics, and elastic moduli of amphibole-rich rocks. J. Geophys. Res. 118, 4699–4728. http://dx.doi.org/10.1002/jgrb.50352.

Jones, C.H., Phinney, R.A., 1998. Seismic structure of the lithosphere from teleseismic converted arrivals observed at small arrays in the southern Sierra Nevada and vicinity, California. J. Geophys. Res. 103, 10065–10090.

Langston, C.A., 1977. The effect of planar dipping structure on source and receiver responses for constant ray parameter. Bull. Seismol. Soc. Am. 67, 1029–1050.

Langston, C.A., 2011. Wave-field continuation and decomposition for passive seismic imaging under deep unconsolidated sediments. Bull. Seis. Soc. Am. 101, 2176–2190. http://dx.doi.org/10.1785/0120100299.

Leidig, M., Zandt, G., 2003. Modeling of highly anisotropic crust and application to the Altiplano–Puna volcanic complex of the central Andes. J. Geophys. Res. 108, 2014.

Levin, V., Park, J., 1997. Crustal anisotropy in the Ural Mountains foredeep from teleseismic receiver functions. Geophys. Res. Lett. 24 (11), 1283–1286.

Levin, V., Park, J., 1998. P–SH conversions in layered media with hexagonally symmetric anisotropy: A CookBook. Pure Appl. Geophys. 151, 669–697.

Levin, V., Margheriti, L., Park, J., Amato, A., 2002a. Anisotropic seismic structure of the lithosphere beneath the Adriatic coast of Italy constrained with mode-converted body waves. Geophys. Res. Lett. 29, 2058.

Levin, V., Park, J., Brandon, M., Lees, J., Peyton, V., Gordeev, E., Ozerov, A., 2002b. Crust and upper mantle of Kamchatka from teleseismic receiver functions. Tectonophysics 358, 233–265.

Levin, V., Roecker, S., Graham, P., Hosseini, A., 2008. Seismic anisotropy indicators in Western Tibet: Shear wave splitting and receiver function analysis. Tectonophysics 462, 99–108.

Ligorria, J.P., Ammon, C.J., 1999. Iterative deconvolution and receiver-function estimation. Bull. Seismol. Soc. Am. 89, 1395–1400.

Lin, F.C., Ritzwoller, M.H., Yang, Y., Moschetti, M.P., Fouch, M.J., 2011. Complex and variable crustal and uppermost mantle seismic anisotropy in the western United States. Nat. Geosci. 4 (1), 55–61.

Liu, H., Niu, F., 2012. Estimating crustal seismic anisotropy with a joint analysis of radial and transverse receiver function data. Geophys. J. Int. 188 (1), 144–164.

Lloyd, G.E., Butler, R.W.H., Casey, M., Mainprice, D., 2009. Mica, deformation fabrics and the seismic properties of the continental crust. Earth Planet. Sci. Lett. 288, 320–328.

Long, M., Silver, P., 2009. Shear wave splitting and mantle anisotropy: Measurements, interpretations, and new directions. Surv. Geophys. 30, 407–461.

McCormack, K., Wirth, E.A., Long, M.D., 2013. B-type olivine fabric and mantle wedge serpentinization beneath the Ryukyu arc. Geophys. Res. Lett. 40, 1697–1702.

McNamara, D., Owens, T.J., 1993. Azimuthal shear wave velocity anisotropy in the Basin and Range province using Moho Ps converted phases. J. Geophys. Res. 98, 12,003–12,017.

Mercier, J.-P., Bostock, M.G., Audet, P., Gaherty, J.B., Garnero, E.J., Revenaugh, J., 2008. The teleseismic signature of fossil subduction: Northwestern Canada. J. Geophys. Res. 113, B04308.

Moschetti, M.P., Ritzwoller, M.H., Lin, F.C., 2010. Seismic evidence for widespread crustal deformation caused by extension in the western USA. Nature 464 (7290), 885–889.

Nagaya, M., Oda, H., Kamimoto, T., 2011. Regional variation in shear-wave polarization anisotropy of the crust in southwest Japan as estimated by splitting analysis of Ps-converted waves on receiver functions. Phys. Earth Planet. Inter. 187, 56–65.

Nikulin, A., Levin, V., Park, J., 2009. Receiver function study of the Cascadia megathrust: Evidence for localized serpentinization. Geochem. Geophys. Geosyst. 10, Q07004.

Obrebski, M., Castro, P.R., 2008. Seismic anisotropy in northern and central Gulf of California region, Mexico, from teleseismic receiver functions and new evidence of possible plate capture. J. Geophys. Res. 113, B03301.

Ozacar, A., Zandt, G., 2009. Crustal structure and seismic anisotropy near the San Andreas Fault at Parkfield, California. Geophys. J. Int. 178, 1098–1104.

Park, J., Levin, V., 2002. Seismic anisotropy: Tracing plate dynamics in the mantle. Science 296, 485–489.

Peng, X., Humphreys, E.D., 1997. Moho Dip and crustal anisotropy in Northwestern Nevada from teleseismic receiver functions. Bull. Seismol. Soc. Am. 87, 745–754.

Phinney, R.A., 1964. Structure of the Earth's crust from spectral behavior of long-period body waves. J. Geophys. Res. 69, 2997–3017.

Porter, R., Zandt, G., McQuarrie, N., 2011. Pervasive lower-crustal seismic anisotropy in Southern California: Evidence for underplated schists and active tectonics. Lithosphere 3, 201–220.

Randall, G.E., 1994. Efficient calculation of complete differential seismograms for laterally homogeneous Earth models. Geophys. J. Int. 118 (1), 245–254. http://dx.doi.org/10.1111/j.1365-246X.1994.tb04687.x.

Reed Jr., G.E., Wheeler, J.O., Tucholke, B.E., 2005. Geologic map of North America. Decade of North American Geology (DNAG) project. Geological Society of America.

Rieger, D.M., Park, J.J., 2012. Forward modeling of quasi-Love scattered-surface waves: Investigating their dependence on seismic anisotropy. In: 2012 Fall Meeting. AGU, San Francisco, Calif., pp. 3–7. Abstract DI24A-06.

Rieger, D.M., Park, J., submitted for publication. The dependence of quasi-Love surface-wave scattering on the orientation of anisotropy and its implications for detecting mantle flow. Geochem. Geophys. Geosyst.

Roselli, P., Agostinetti, N.P., Braun, T., 2010. Shear-velocity and anisotropy structure of a retreating extensional forearc (Tuscany, Italy) from receiver functions inversion. Geophys. J. Int. 181, 545–556.

Savage, M.K., 1998. Lower crustal anisotropy or dipping boundaries? Effects on receiver functions and a case study in New Zealand. J. Geophys. Res. 103, 15,069–15,087.

Savage, M.K., 1999. Seismic anisotropy and mantle deformation: What have we learned from shear wave splitting?. Rev. Geophys. 37 (1), 64–106.

Schulte-Pelkum, V., Blackman, D.K., 2003. A synthesis of seismic P and S anisotropy. Geophys. J. Int. 154, 166–178.

Schulte-Pelkum, V., Monsalve, G., Sheehan, A., Pandey, M.R., Sapkota, S., Bilham, R., Wu, F., 2005. Imaging the Indian subcontinent beneath the Himalaya. Nature 435, 1222–1225.

Shen, W., Ritzwoller, M.H., Schulte-Pelkum, V., Lin, F.-C., 2013a. Joint inversion of surface wave dispersion and receiver functions: A Bayesian Monte-Carlo approach. Geophys. J. Int. 192, 807–836. http://dx.doi.org/10.1093/gji/ggs050.

Shen, W., Ritzwoller, M.H., Schulte-Pelkum, V., 2013b. A 3-D model of the crust and uppermost mantle beneath the central and western US by joint inversion of receiver functions and surface wave dispersion. J. Geophys. Res. 118, 1–15. http://dx.doi.org/10.1029/2012JB009602.

Shen, W., Ritzwoller, M.H., Schulte-Pelkum, V., 2013c. Crustal and uppermost mantle structure in the central U.S. encompassing the Midcontinent Rift. J. Geophys. Res. 118, 4325–4344. http://dx.doi.org/10.1002/jgrb.50321.

Sherrington, H.F., Zandt, G., Frederiksen, A., 2004. Crustal fabric in the Tibetan Plateau based on waveform inversions for seismic anisotropy parameters. J. Geophys. Res. 109, B02312.

Shiomi, K., Park, J., 2008. Structural features of the subducting slab beneath the Kii Peninsula, central Japan: seismic evidence of slab segmentation, dehydration, and anisotropy. J. Geophys. Res. 113, B10318.

Smithson, S.B., Brewer, J.A., Kaufman, S., Oliver, J.E., Hurich, C.A., 1979. Structure of the Laramide Wind River uplift, Wyoming, from COCORP deep reflection data and from gravity data. J. Geophys. Res. 84, 5955–5972.

Song, T., Kim, Y., 2012. Localized seismic anisotropy associated with long-term slow-slip events beneath southern Mexico. Geophys. Res. Lett. 39, L09308.

Steidtmann, J.R., Middleton, L.T., 1991. Fault chronology and uplift history of the southern Wind River Range, Wyoming: Implications for Laramide and post-Laramide deformation in the Rocky Mountain foreland. Geol. Soc. Am. Bull. 103, 472–485.

Stone, D.S., 1987. Wyoming Transect A; Regional Geological Cross Sections: Rocky Mountain Transects, Littleton, Colorado.

Tatham, D.J., Lloyd, G.E., Butler, R.W.H., Casey, M., 2008. Amphibole and lower crustal seismic properties. Earth Planet. Sci. Lett. 267, 118–128.

Please cite this article in press as: Schulte-Pelkum, V., Mahan, K.H. A method for mapping crustal deformation and anisotropy with receiver functions and first results from USArray. Earth Planet. Sci. Lett. (2014), http://dx.doi.org/10.1016/j.epsl.2014.01.050

Vergne, J., Wittlinger, G., Farra, V., Su, H., 2003. Evidence for upper crustal anisotropy in the Songpan–Ganze (northeastern Tibet) terrane. Geophys. Res. Lett. 30.

Vinnik, L.P., 1977. Detection of waves converted from P to SV in the mantle. Phys. Earth Planet. Inter. 15, 39–45.

Ward, D., Mahan, K., Schulte-Pelkum, V., 2012. Roles of quartz and mica in seismic anisotropy of mylonites. Geophys. J. Int. 190 (2), 1123–1134.

Wessel, P., Smith, W.H.F., 1998. New, improved version of generic mapping tools released. Eos Trans. AGU 79 (47), 579.

Whitmeyer, S.J., Karlstrom, K., 2007. Tectonic model for the Proterozoic growth of North America. Geosphere 3, 220–259. http://dx.doi.org/10.1130/GES00055.1.

Wirth, E.A., Long, M., 2012. Multiple layers of seismic anisotropy and a low-velocity region in the mantle wedge beneath Japan: Evidence from teleseismic receiver functions. Geochem. Geophys. Geosyst. 13, Q08005.

Zandt, G., Gilbert, H., Owens, T.J., Ducea, M., Saleeby, J., Jones, C.H., 2004. Active foundering of a continental arc root beneath the southern Sierra Nevada in California. Nature 431, 41–46.

Please cite this article in press as: Schulte-Pelkum, V., Mahan, K.H. A method for mapping crustal deformation and anisotropy with receiver functions and first results from USArray. Earth Planet. Sci. Lett. (2014), http://dx.doi.org/10.1016/j.epsl.2014.01.050

Supplementary Information

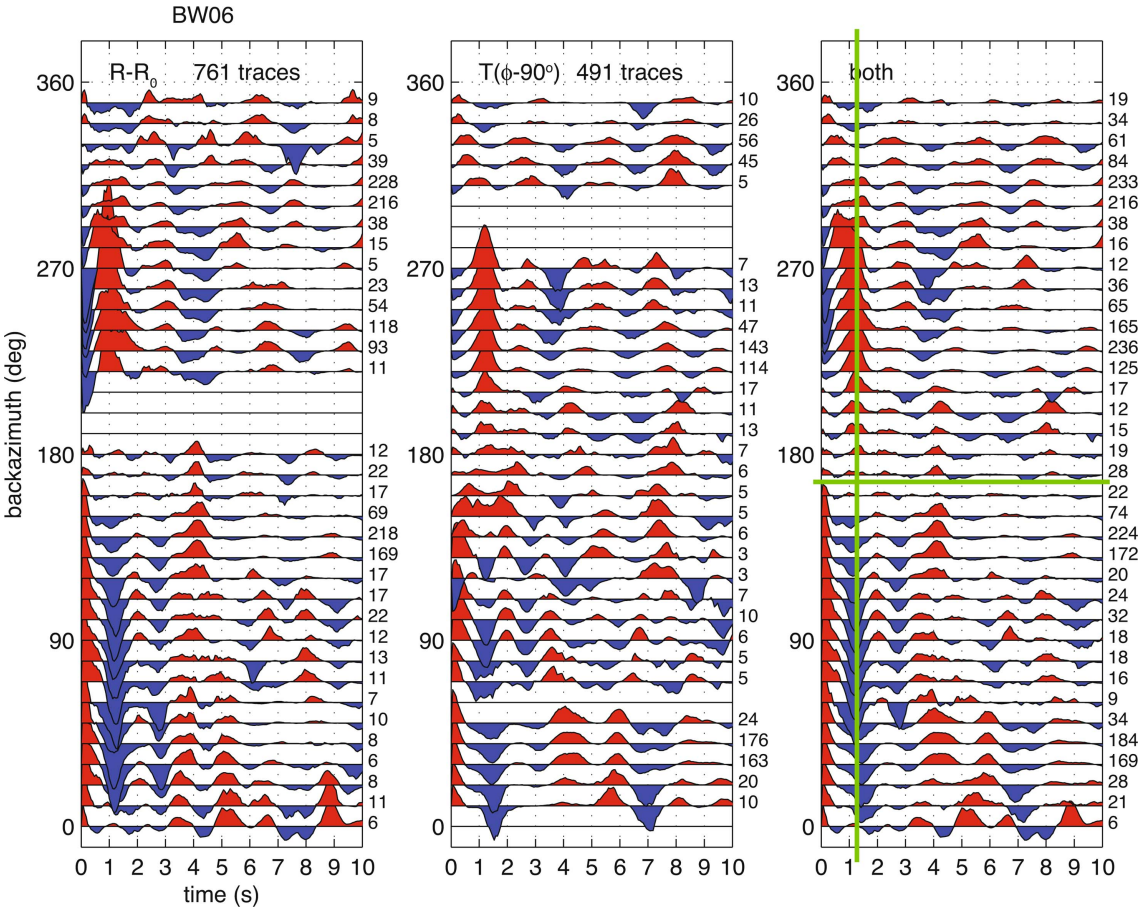

Fig. S1: Same as Fig. 7, but for station BW06.

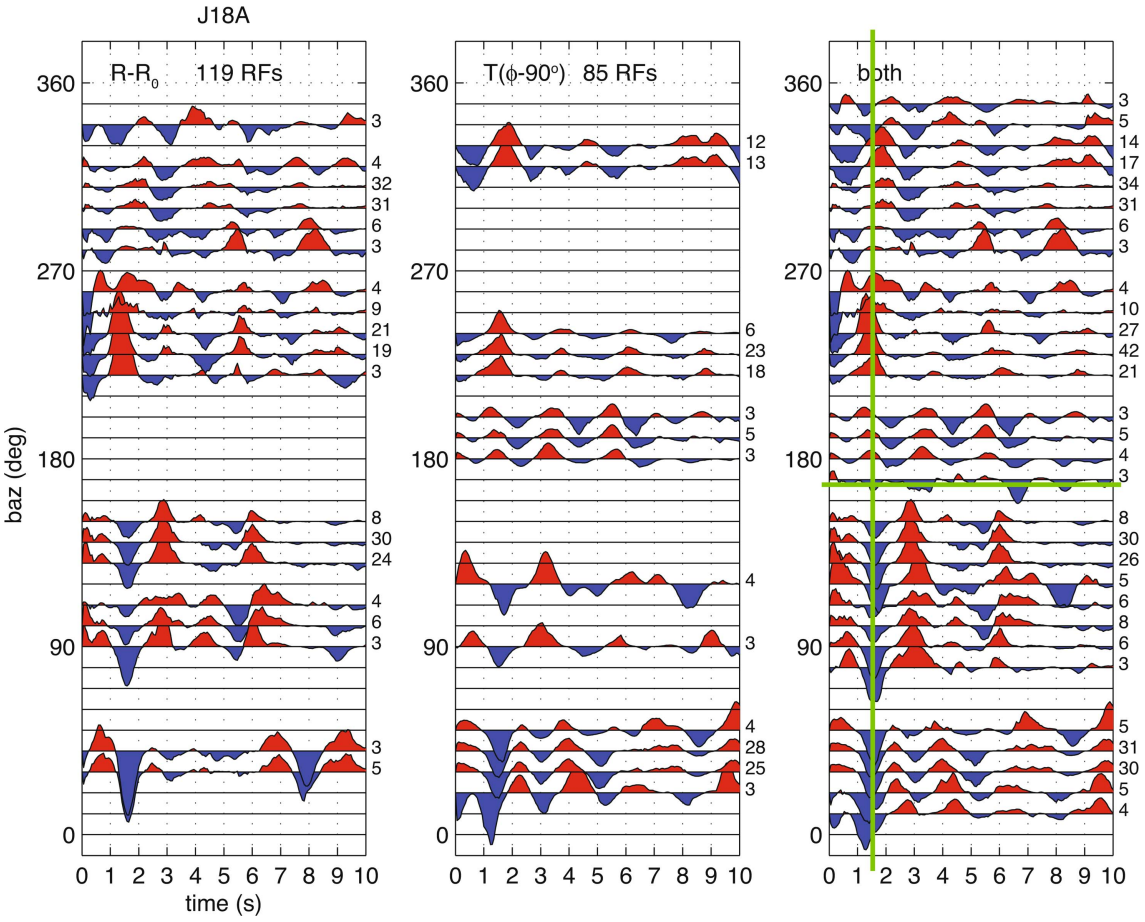

Fig. S2: Same as Fig. 7, but for station J18A.

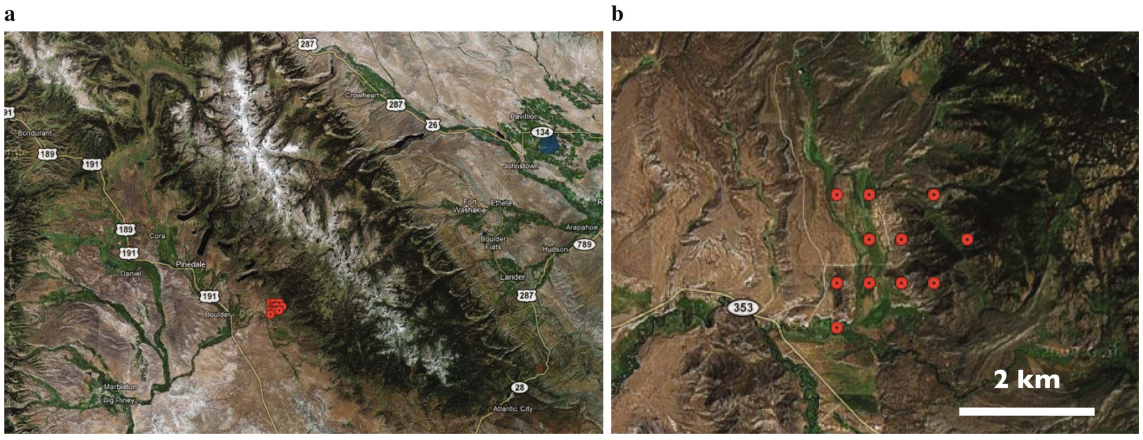

Fig. S3: PDAR array map.

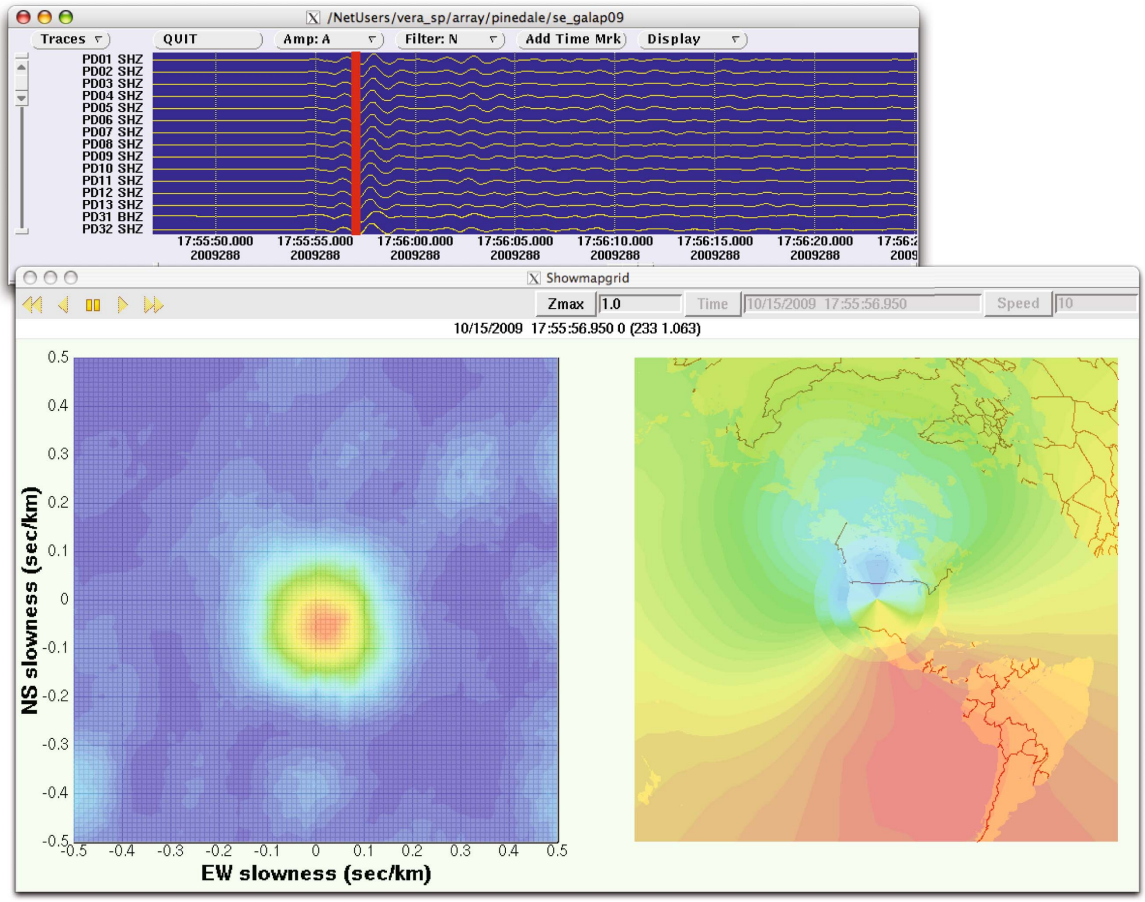

Fig. S4: (top) PDAR vertical component for P arrival of example event used in beamforming and f-k analysis to test for lateral scattering. (bottom) f-k grid showing steeply incident energy for a time window of 1 s starting at the red line in the trace plot above, shown in slowness space (left) and in a geographic projection (right). Hot colors show high beam energy, cool colors low. The slowness and azimuth correspond to the correct teleseismic source location near Galapagos and shows no suggestion of laterally scattered energy.

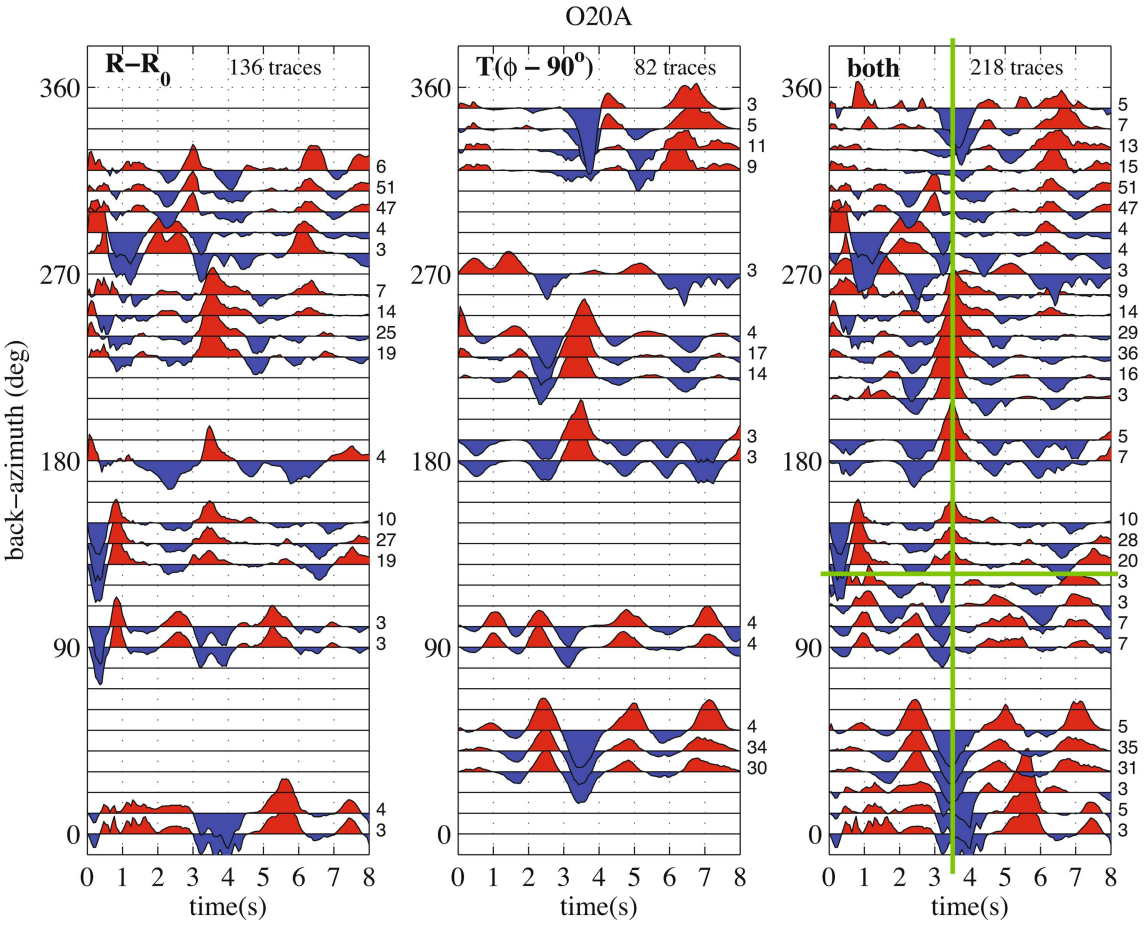

Fig. S5: Same as Fig. 7, but for station O20A. The lack of a degree-2 direct P arrival near zero time suggests plunging axis anisotropy.

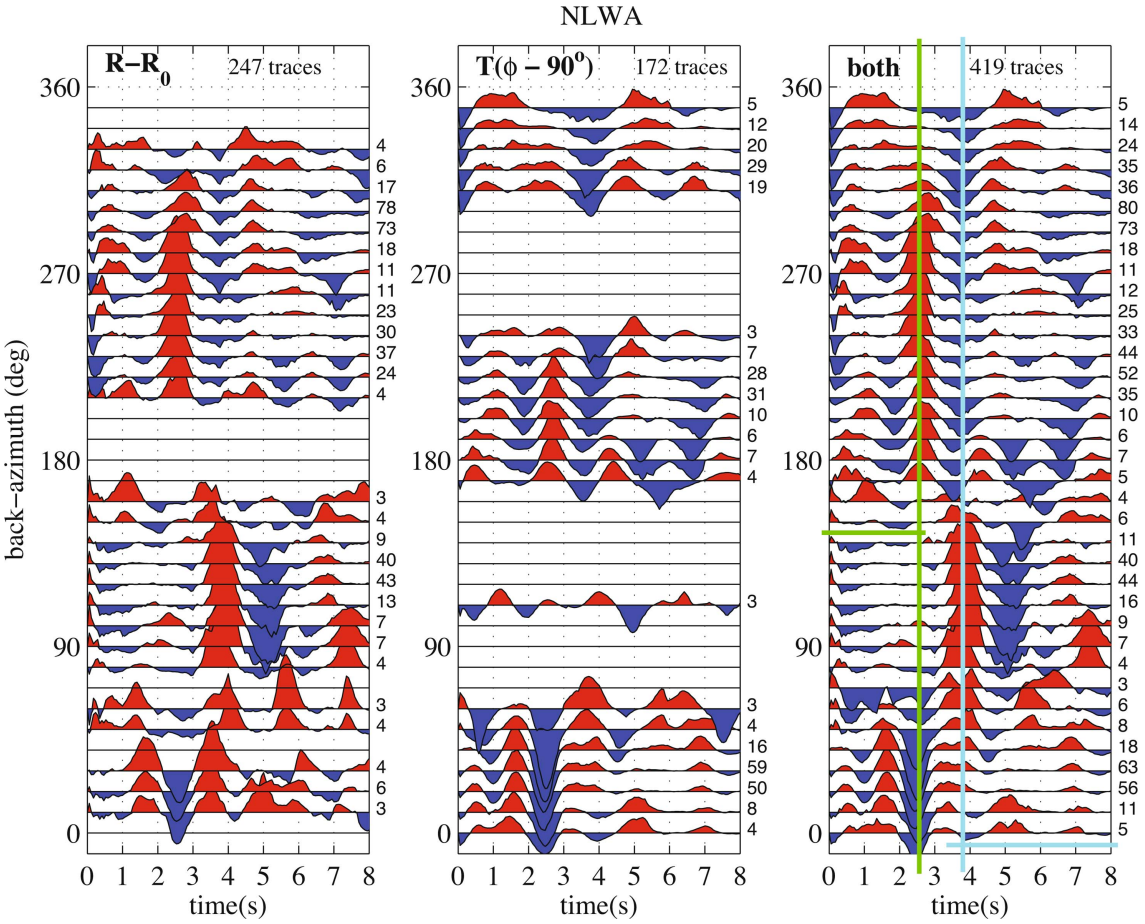

Fig. S6: Same as Fig. S5, but for station NLWA.

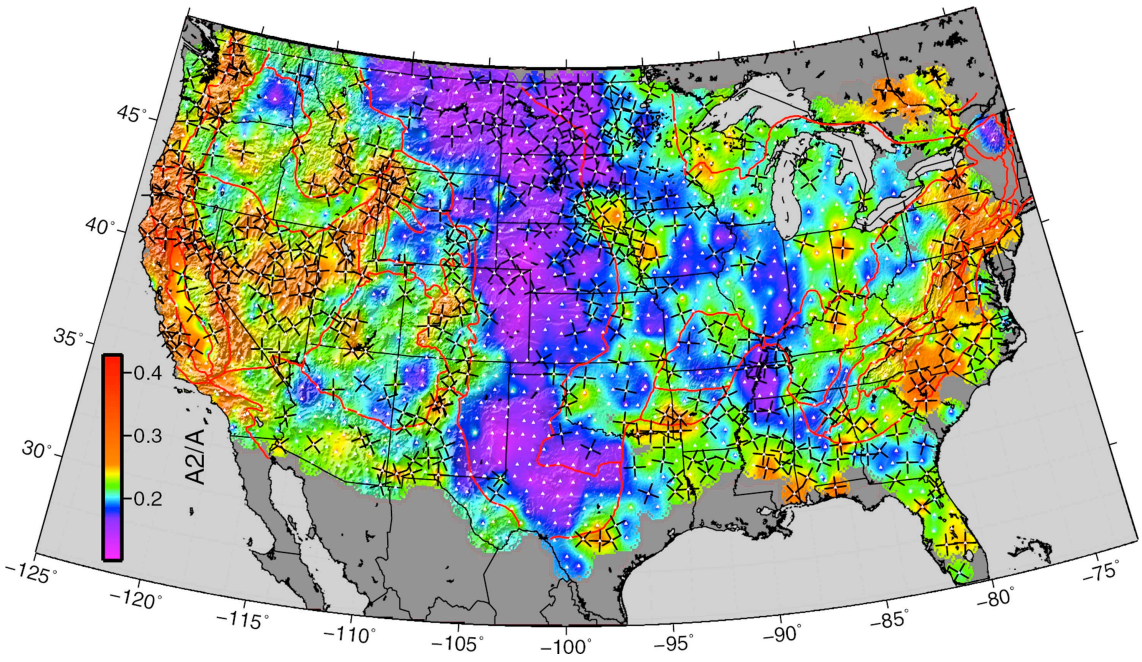

Fig. S7: Same as Fig. 8, but color showing the degree-2 signal amplitude (attributable to azimuthal anisotropy) rather than degree-1 amplitude averaged from 0-8 s, normalized by total amplitude from 0-8 s. Color scale is A2/A ratio. Black crosses show orientation of fast or slow symmetry axis and the plane perpendicular to it.